

**REPORT DOCUMENTATION PAGE**

AFRL-SR-BL-TR-01-

Public reporting burden for this collection of information is estimated to average 1 hour per response, including the time for reviewing the data needed, and completing and reviewing this collection of information. Send comments regarding this burden estimate or any of reducing this burden to Washington Headquarters Services, Directorate for Information Operations and Reports, 1215 Jefferson Davis Management and Budget, Paperwork Reduction Project (0704-0188), Washington, DC 20503

1. AGENCY USE ONLY (Leave blank)

2. REPORT DATE

15 December 2000

3. REPORT TYPE AND DATES COVERED

Final Report, 1 Apr 1999 - 30 Apr 2000

4. TITLE AND SUBTITLE

Flow Diagnostic Instrumentation For Turbulent Flow Studies

5. FUNDING NUMBERS

AFOSR DURIP

Grant F49620-99-1-0181

6. AUTHOR(S)

C. Randall Truman

7. PERFORMING ORGANIZATION NAME(S) AND ADDRESS(ES)

Mechanical Engineering Department  
University of New Mexico  
Albuquerque NM 87131

8. PERFORMING ORGANIZATION  
REPORT NUMBER

9. SPONSORING / MONITORING AGENCY NAME(S) AND ADDRESS(ES)

AFOSR/NA  
801 N. Randolph St Room 732  
Arlington VA 22203-1977

10. SPONSORING / MONITORING  
AGENCY REPORT NUMBER

11. SUPPLEMENTARY NOTES

12a. DISTRIBUTION / AVAILABILITY STATEMENT

Unlimited

AIR FORCE OFFICE OF SCIENTIFIC RESEARCH (AFOSR)  
NOTICE OF TRANSMITTAL DTIC. THIS TECHNICAL REPORT  
HAS BEEN REVIEWED AND IS APPROVED FOR PUBLIC RELEASE  
LAW AFR 190-12. DISTRIBUTION IS UNLIMITED.

13. ABSTRACT (Maximum 200 Words)

Flow diagnostic instrumentation to measure turbulent flow in research and instructional wind tunnels was acquired. These instruments include a multi-channel hot-wire anemometer and a recently developed optical analysis system based on a two-dimensional Hartmann sensor. Four CTA channels for velocity and two CCA channel for temperature are included. The optical analysis system includes a PC for acquisition of phase and intensity optical measurements in a two-dimensional array. These systems provide simultaneous measurements of velocity, temperature and optical degradation in turbulent flow. Applications include optical propagation through turbulent shear flows (e.g. Airborne Laser), as well as flow diagnostics for studies of the control of flow separation, transition and turbulence.

20010220 065

14. SUBJECT TERMS

turbulent flow, optical diagnostic, flow control

15. NUMBER OF PAGES

10

16. PRICE CODE

17. SECURITY CLASSIFICATION  
OF REPORT18. SECURITY CLASSIFICATION  
OF THIS PAGE19. SECURITY CLASSIFICATION  
OF ABSTRACT

20. LIMITATION OF ABSTRACT

# FLOW DIAGNOSTIC INSTRUMENTATION FOR TURBULENT FLOW STUDIES

AFOSR DURIP Grant F49620-99-1-0181, 01 Apr 99 – 30 Apr 00

Prof. C. Randall Truman  
Department of Mechanical Engineering  
University of New Mexico  
Albuquerque, NM 87131

This report is drawn from interim reports to the NASA PURSUE program at the University of New Mexico and an AIAA Region IV Student Conference Paper, "Design Of An Optical Diagnostic For Turbulent Shear Flows," by Pat Chavez, graduate student supported by an AFOSR AASERT grant.

## Abstract

Optical phasefront propagation through turbulent flow has become an established method of analyzing turbulent structures without disrupting the flow field. The Shack-Hartmann wavefront sensor is an array of lenslets, each of which focuses a very small section of an incoming laser beam onto a CCD array. The displacement of each focal spot in reference to the spot produced from a collimated beam is a measure of phase shift; this distribution can then be integrated to reconstruct the total phasefront. The distortion of the incident laser beam is related to turbulent structure in the flow. An optical system has been designed around a wind tunnel that incorporates such a sensor to study turbulent shear flows. Preliminary analysis will be performed for a plane-mixing layer to understand the type of phasefront signature to be expected from a turbulent free shear layer. This technique will be extended to the study of flow control using deformable surface airfoils.

## Introduction

Many aspects of modern flight rely on the control of flow over surfaces, from airplane wings to jet turbine blades. Controlling the effect of these surfaces on the flow and hence the flow's effect on the surface is paramount in design. Design criteria are often established by computers but these models must be benchmarked against experimental data in order to be reliable. Of the many diagnostic methods currently available, non-intrusive optical diagnostic methods offer several advantages. Principally the absence of any instrumentation within the flow allows data acquisition to be performed without disrupting the flow in any way. Secondly, very rapid fluctuations can be analyzed with optical techniques and small length scales can be resolved. All of these advantages make optical diagnostic techniques prime candidates for the analysis of turbulent flow.

A few common optical diagnostic techniques are Laser Doppler Velocimetry, Particle Image Velocimetry, Planar Laser Induced Fluorescence<sup>1</sup> and the use of a Shack-Hartmann (or Hartmann) Wavefront Sensor. In this research project it is necessary to analyze turbulent flow with high frequency fluctuations and fine-scale features. The Shack-Hartmann Wavefront Sensor has been selected as the appropriate optical diagnostic.

## Background

### Hartmann Wavefront Sensor<sup>2</sup>

The Hartmann wavefront sensor is an optical diagnostic tool that operates by measuring the change in optical phase of a collimated laser beam that has propagated through a flowfield. When a collimated laser source is propagated through an aberrating medium such as turbulent flow, the non-uniformity of the density field distorts the incident planar phasefront. Upon exiting the flowfield, the phasefront has been aberrated through changes that equal the path integral of refractive index variations along the optical axis. Figure 1 shows a schematic of propagation through a flow channel with windows.

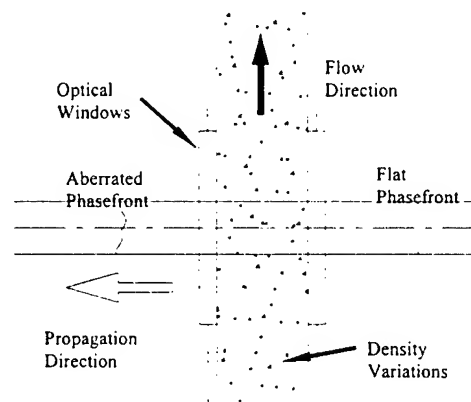


Figure 1 – Phasefront Aberration

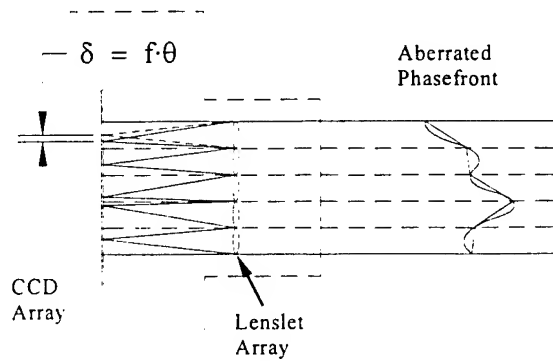


Figure 2 – Displacement of Focal Spot

The critical element of the Hartmann sensor is the lenslet array; in this case it is a two-dimensional array of very small lenses (order  $\sim 0.1$  mm  $\varnothing$ ) that focus the aberrated phasefront onto a charge-coupled device (CCD) array or camera. The focal spot location is dependent upon the local incident phasefront angle of the discretized laser beam. The reference spot location is taken to be the location of the spot formed by a planar phasefront, i.e., with a collimated beam. The difference in spot location is directly related to the average incident angle of the local aberrated phasefront, employing the small angle approximation. Figure 2 shows a cross-sectional view of the Hartmann sensor, note the relation between the focal length of the lenslets  $f$ , displacement  $\delta$  and the local phasefront angle  $\theta$ . This spot location is calculated in both the  $x$  and  $y$  directions (for optic axis in  $z$  direction) by the accompanying software and integrated to reconstruct the 2-D phasefront<sup>2</sup>. The aberration of the incident laser beam is related to turbulent structures in the flow.

#### Relay – Imaging Optics

Because the Hartmann sensor has such a small aperture, approximately 6 mm by 4 mm, it becomes necessary to incorporate a relay-imaging optical system in order to increase the size of the laser beam through the test section to the scale of typical flow structures. Relay-imaging optics act as a magnification instrument. By propagating light through a series of two lenses of different focal lengths, an image is magnified by the ratio of the focal lengths. One very interesting aspect of this instrument is that not only is the beam diameter magnified but the optical phase deviation, or tilt of the laser beam is also inversely magnified. Figure 3 depicts this dual characteristic of relay-imaging lenses.

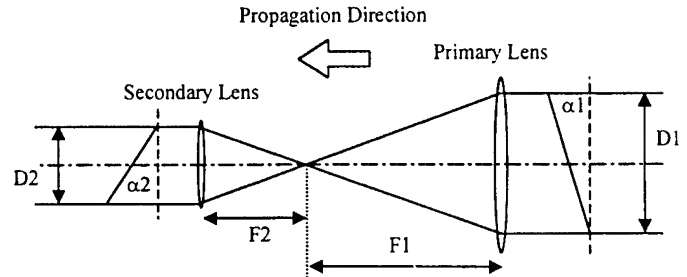


Figure 3 – Relay-Imaging Optics

For propagation to the left, the magnification  $M$  is defined by

$$M = \frac{F2}{F1} \quad (1)$$

The diameter of the laser beam changes according to

$$D2 = M \cdot D1 \quad (2)$$

where  $D1$  is the beam diameter through the wind tunnel and  $D2$  is the beam diameter entering the Hartmann sensor. The phase angle is altered according to

$$\alpha2 = \frac{\alpha1}{M} \quad (3)$$

These relationships serve our needs in two ways. By mandating a magnification parameter of less than unity (de-magnifying the beam diameter) it is possible to observe larger regions of the flow while at the same time increasing the sensitivity to phase deviation by magnifying the localized phase angles.

#### Experimental Setup

##### Wind Tunnel

The wind tunnel used in this research was manufactured for use at the Air Force Phillips Laboratory for research pertaining to optical propagation through turbulent shear flow. Heated walls were used to develop index of refraction fluctuations to simulate compressible turbulent flow over an aircraft. It was dubbed the Turbulent Boundary Layer Generator, or TBLG. Figures 4a and 4b show diagrams of the facility.

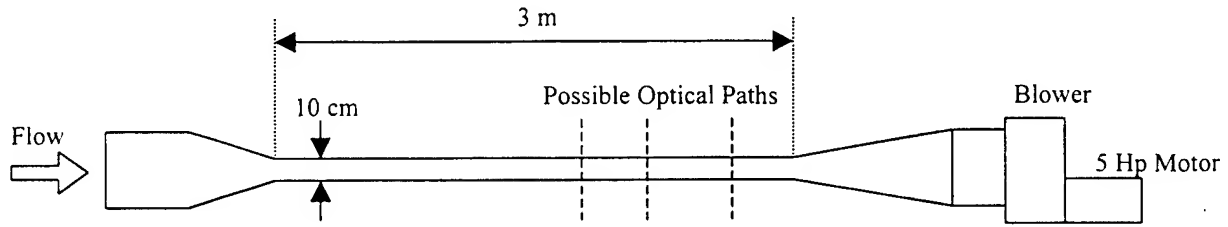


Figure 4a - Top View of TBLG

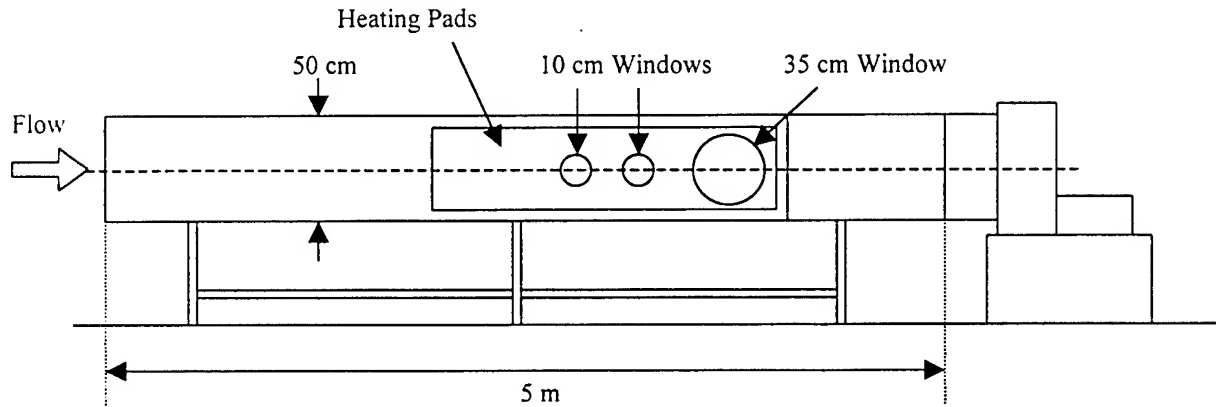


Figure 4b - Side View of TBLG

The power of the motor can be controlled to achieve a large range of test-section velocities ( $\sim 2$ - $36$  m/s) and the sidewall heating pads can be controlled independently up to temperatures of approximately  $120^{\circ}\text{C}$ . Along the top of the wind tunnel there are 7 probe access holes. Of those, 4 are located in the test section with special probe traversing capability. Along one of the sidewalls, there are 12 probe-traversing stations at 4 streamwise locations, as shown in Figure 5.

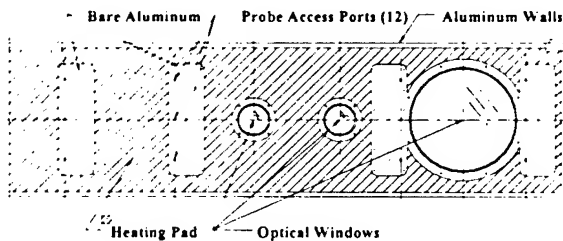


Figure 5 - TBLG Test Section Profile

#### Hartmann Wavefront Sensor

The Hartmann sensor is comprised of a laser source, optical train, lenslet array and a receiving camera. These optical components are mounted on two independent supports on each side of the TBLG as shown in Figure 6. A milling machine base serves as a support for the laser source and a 2 ft x 3 ft breadboard is used to mount the relay-imaging lenses and camera.

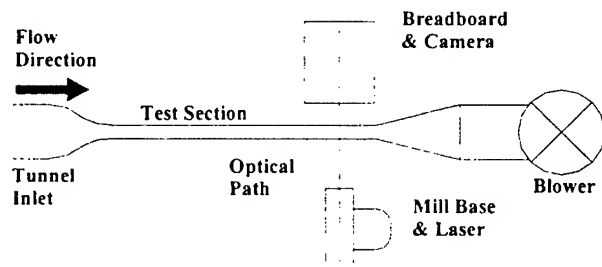


Figure 6 - Overall Setup

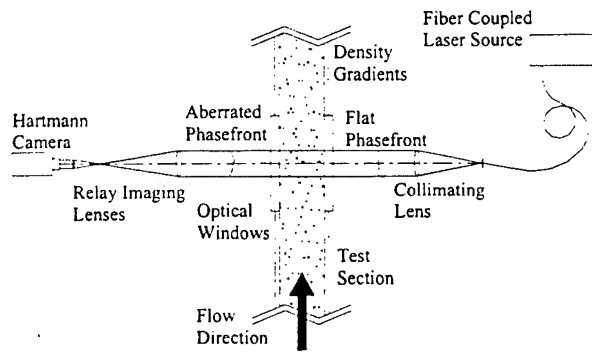


Figure 7 – Optical Arrangement

Because a large beam diameter for propagation through the flow was desired, a point source collimated by a large convex lens was chosen. This was achieved with a fiber optic pig-tailed to a diode laser source; a 535 nm wavelength unit was purchased complete. In order to yield the most precise collimation it was necessary to use achromatic lenses. These are actually two lenses cemented together to greatly reduce optical aberrations. Once collimated, the beam is propagated through the wind tunnel. The beam diameter is then reduced by relay-imaging lenses to allow passage through the camera aperture. Figure 7 shows the optical setup.

Careful consideration was given to choosing the relay-imaging lenses. This was further complicated with five possible arrays of varying numbers of lenslets. The critical variables in this scenario, spatial resolution and phase angle sensitivity, are determined by the

number of lenslets in the array and the relay-imaging magnification. Resolution is measured in mm per lenslet over the field of view and sensitivity is measured as the minimum phase angle difference that can be detected over each lenslet. It is beneficial to achieve small spatial resolutions and small phase angle sensitivities. The effect of lenslet array size on sensitivity and resolution has a dual nature, because increasing the number of lenslets improves the spatial resolution but degrades the sensitivity. This is illustrated in Figure 8, where a magnification of 1.0 has been assumed.

Figure 8 illustrates that increasing the number of lenslets in the array improves spatial resolution but degrades the sensitivity of the sensor. The number of lenslets in each 2-D array is shown on the figure near the data points. It should be noted that the largest possible beam diameter has been used in calculations for optimum array coverage as illustrated in Figure 9.

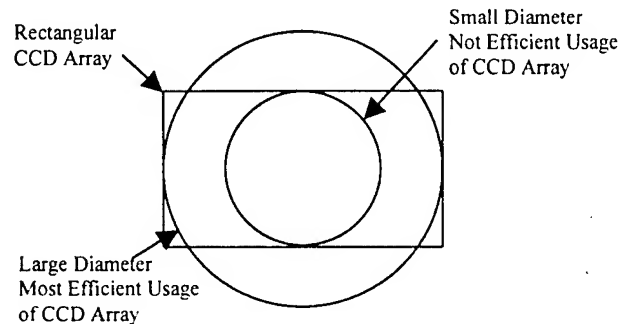


Figure 9 – Beam Coverage of CCD

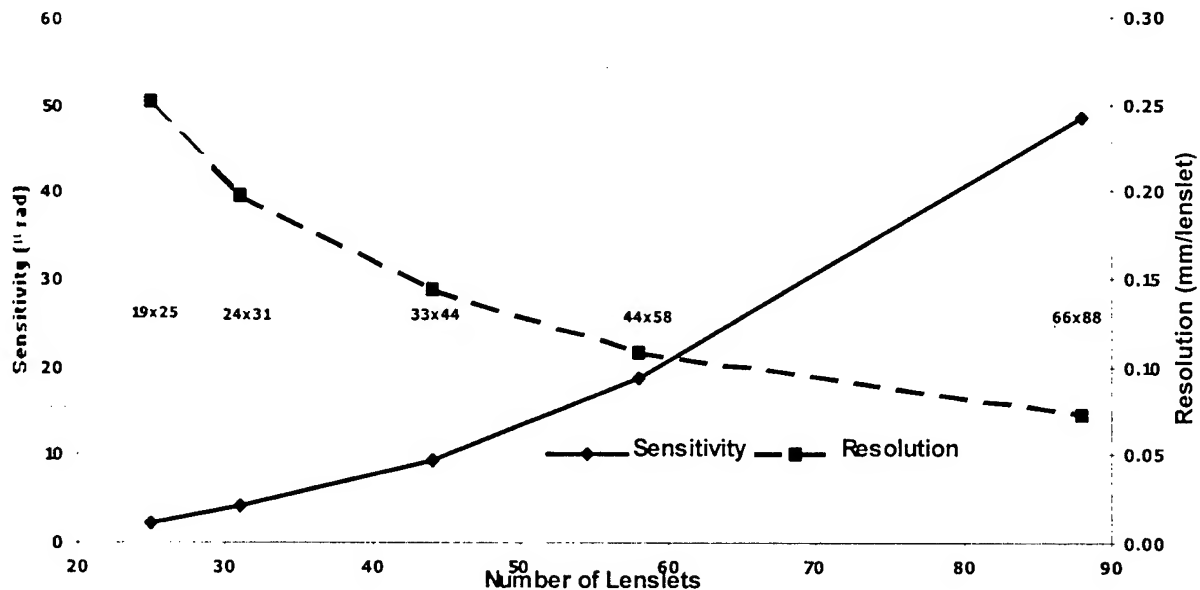


Figure 8 – Sensitivity & Resolution as Function of Lenslet Array Size for M=1

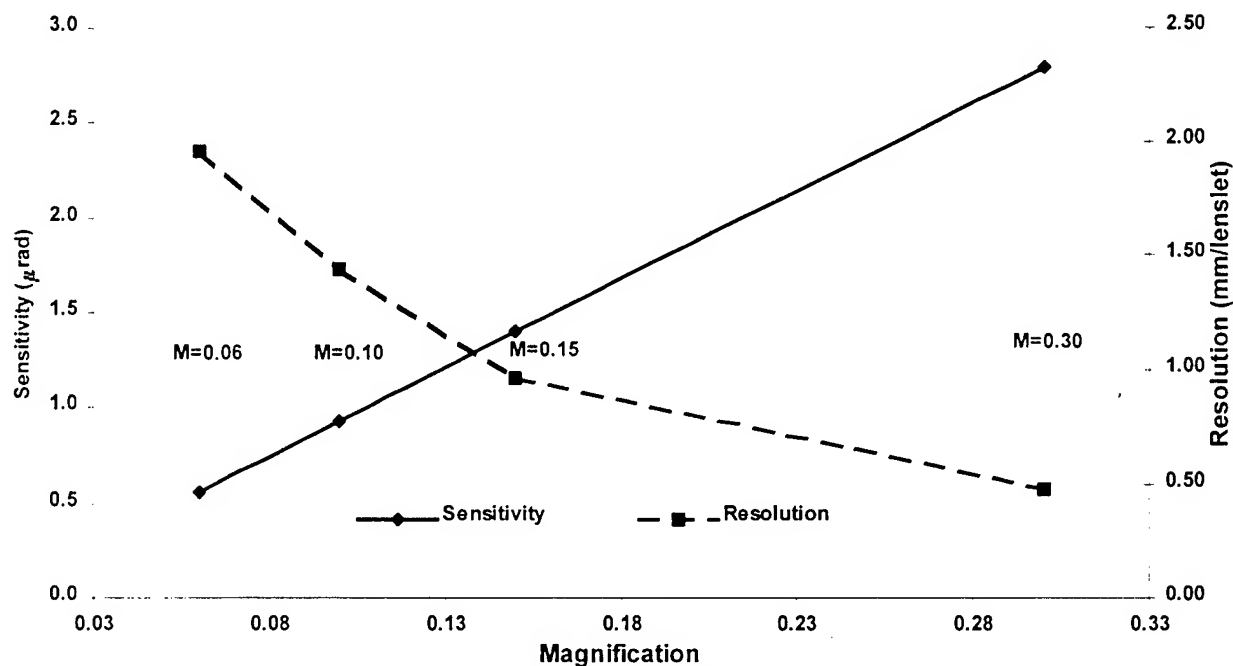


Figure 10 – Sensitivity & Resolution as Function of Magnification for 33 x 44 Lenslet Array

Magnification has a similar effect; as magnification is increased, spatial resolution is again improved while sensitivity is again degraded. Recall that  $M < 1$  (demagnification) reduces the beam diameter to fit the Hartmann sensor aperture. Figure 10 shows this tradeoff of values for the median number of lenslets, 33 x 44; other array sizes display similar behavior.

Most noteworthy is the effect of using the relay-imaging optics. In changing from no magnification ( $M = 1$ ), to  $M = 0.1$ , resolution values increase by a factor of 10. Each lenslet is imaging a region of the flow that is 10 times larger. However, sensitivity values improve by a factor of 10. This holds for any size array, but the 33 x 44 lenslet case can be verified with Figures 8 and 10. The magnification values  $M = 0.06, 0.10, 0.15$  and  $0.30$  correspond to beam diameter through the test section of 4, 3, 2 and 1 inches, respectively. The best solution would have the means of varying the test section beam diameter over a range of sizes, thus varying the spatial resolution to observe particular length scales one at a time. This was achieved by using 3-inch primary lenses with three different secondary lenses of varying focal lengths to produce the desired magnifications. By selecting 3-inch rather than 4-inch lenses, the total cost of lenses was cut in half because large achromatic lenses get very expensive. The median array size, 33 x 44 lenslets, was chosen for its good range of spatial resolution ( $\sim 1 - 2.5$  mm/lenslet) and sensitivity ( $\sim 0.5 - 1.5 \mu\text{rad}$ ). It was not certain at the time what length scales were expected, but since the vendor is local and willing to perform the occasional lenslet array swap, the median array size was a good starting point.

### Simulations

Hartmann sensor data acquisition has not yet been performed on flow control surfaces, so it is not clear how to interpret the phasefront data. The optical diagnostic must first be benchmarked against a well-documented flow pattern in order to establish a set of guidelines relating flow conditions and phasefront signatures. A plane shear layer will be used for this point of reference. A splitter plate will be used to generate the plane shear layer within the TBLG, with one sidewall heated above ambient to mark the flow with a passive scalar (temperature) that can be differentiated with the Hartmann sensor. Similar studies have been performed using a round low-speed heated jet.<sup>3</sup>

In order to best design a splitter plate, some computer modeling has been performed. The primary concern is separation in the splitter plate boundary layer. Since air will be both accelerated and decelerated around the splitter plate, the decelerating side could possibly separate due to the adverse pressure gradient as depicted in Figure 11.

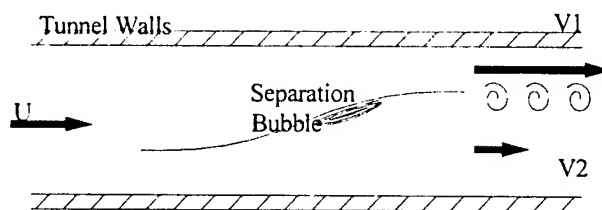


Figure 11  
Separation on Decelerating Side of Splitter Plate

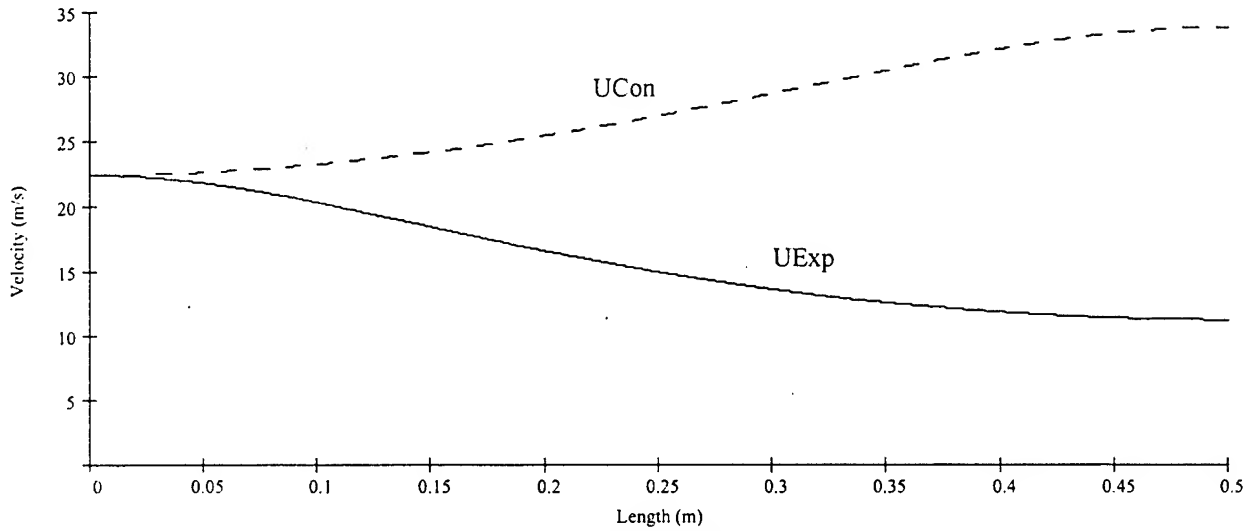


Figure 12 – Splitter Plate Velocities

The ratio of the two final velocities is a characteristic parameter of the mixing layer, called the velocity ratio

$$R = \frac{U_1}{U_2} \quad (4)$$

The magnitude of deceleration determines whether the flow will separate, and is directly related to the velocity ratio. The velocity ratio is in turn determined by the shape and position of the splitter plate within the test section. A 3<sup>rd</sup> order polynomial has been used to specify the shape of the splitter plate and a lateral offset parameter has been incorporated into the equations. Figure 12 shows a velocity distribution along the splitter plate for  $R = 3.0$ .

The expanding (decelerating) and contracting (accelerating) velocities are  $U_{Exp}$  and  $U_{Con}$ , respectively. To predict if separation will occur on the decelerating side, the Head Method<sup>4</sup> is employed to calculate the coefficient of friction along the wall. If this value falls to zero, separation has occurred. The Head Method for a turbulent boundary layer is a system of five equations, two of which are differential equations. The system of equations based on momentum and energy balances and correlations for boundary layer variables is

$$\frac{d}{dx}(U \cdot \theta \cdot H_1) = U \cdot F \quad (5a)$$

$$F = 0.0306(H_1 - 3.0)^{-0.6169} \quad (5b)$$

$$H_1 = \begin{cases} 0.8234(H - 1.1)^{-1.287} + 3.3 & H \leq 1.6 \\ 1.5501(H - 0.6778)^{-3.064} + 3.3 & H \geq 1.6 \end{cases} \quad (5c)$$

$$\frac{d\theta}{dx} + (H + 2)\frac{\theta}{U} \frac{dU}{dx} = \frac{c_f}{2} \quad (5d)$$

$$c_f = 0.246 \times 10^{-0.678H} \text{Re}_\theta^{-0.268} \quad (5e)$$

where Reynolds number based on momentum thickness is defined as

$$\text{Re}_\theta = \frac{U \cdot \theta}{\nu} \quad (6)$$

Two of the three quantities  $\theta$ ,  $H$  or  $c_f$  must be specified as initial conditions; these values are obtained with a laminar boundary layer model. The laminar flow model used is Thwaites' Method<sup>5</sup>, an integral method that determines the momentum thickness as a function of velocity. Given  $U(x)$ , the streamwise velocity distribution, the momentum thickness  $\theta$  is obtained from

$$\theta^2 = \frac{0.45\nu}{U^6} \int_0^x U^5 dx \quad (7)$$

The shape factor  $H$ , is calculated from

$$\lambda = \frac{\theta^2}{\nu} \frac{dU}{dx} \quad (8)$$

$$H = 4576z^5 - 3337z^4 + 854z^3 - 835z^2 + 4.14z + 2 \quad (9)$$

where  $z = 0.25 - \lambda$ . The parameters  $\theta$  and  $H$  are evaluated at the onset of transition to turbulence and used as initial data for the Head Method calculation. In order to locate the point of transition to turbulence, the

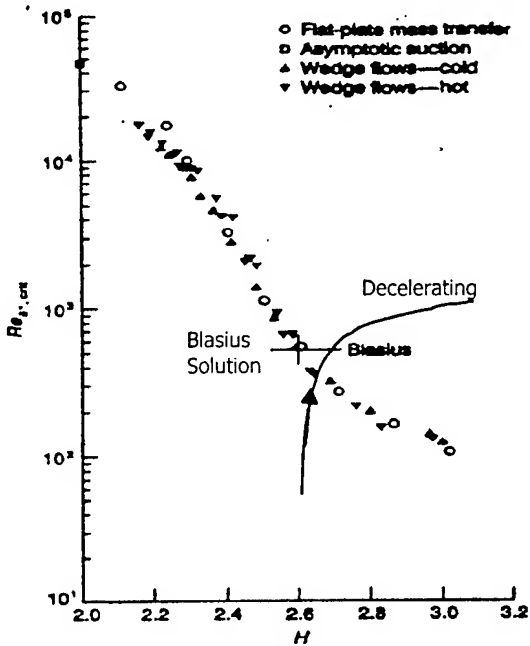


Figure 13

Reynolds number based on displacement thickness at onset of transition to turbulence vs. boundary layer shape factor. Taken from Reference 5.

Reynolds number based on displacement thickness  $Re_{\delta^*}$  was compared to a correlation for critical  $Re_{\delta^*}$  vs. shape factor  $H$ , shown in Figure 13. Also shown is the approximate path and point of transition to turbulence at ~6% length along the splitter plate.

Similar calculations to predict boundary layer growth within the wind tunnel up to the splitter plate position have not yet been completed. These calculations will eventually incorporate thermal boundary layer correlations, which will aid in choosing the offset placement of the splitter plate. Due to the

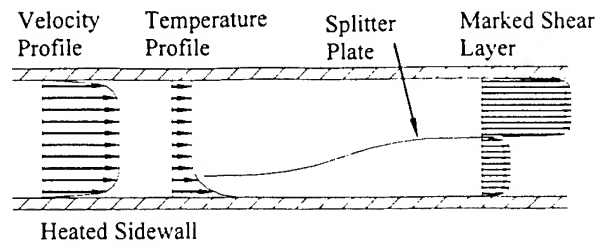


Figure 14 – Optimal Splitter Plate Location

location of the heating pads well into the test-section, the thermal boundary layer will begin to develop much further downstream than the velocity boundary layer. It will grow at approximately the same rate since the Prandtl number for air is approximately unity,  $Pr \approx 1$ . While the velocity boundary layer is nearly fully developed at the splitter plate, the thermal boundary layer (on one sidewall) will still be growing. With proper shape and offset of the splitter plate, the thermal boundary layer would be contained to one side of the splitter plate, ensuring adequate temperature difference across the shear layer for the Hartmann sensor. This orientation could also position the trailing edge of the splitter plate, and ensuing shear layer, as close as possible to the wind tunnel centerline solving a separate but related problem. A shear layer along the centerline would minimize interaction with sidewall boundary layers as far downstream as possible. An estimated location of the splitter plate is illustrated in Figure 14.

The predictions for this splitter plate configuration are promising. Figure 15 shows the output parameters of the Head Method for a case designed to prevent separation vs. splitter plate length. The splitter plate length is 0.5m, the velocity ratio is 3.0 and the lateral offset is 1.25cm towards the decelerating (expanding) side as shown in Figure 14.

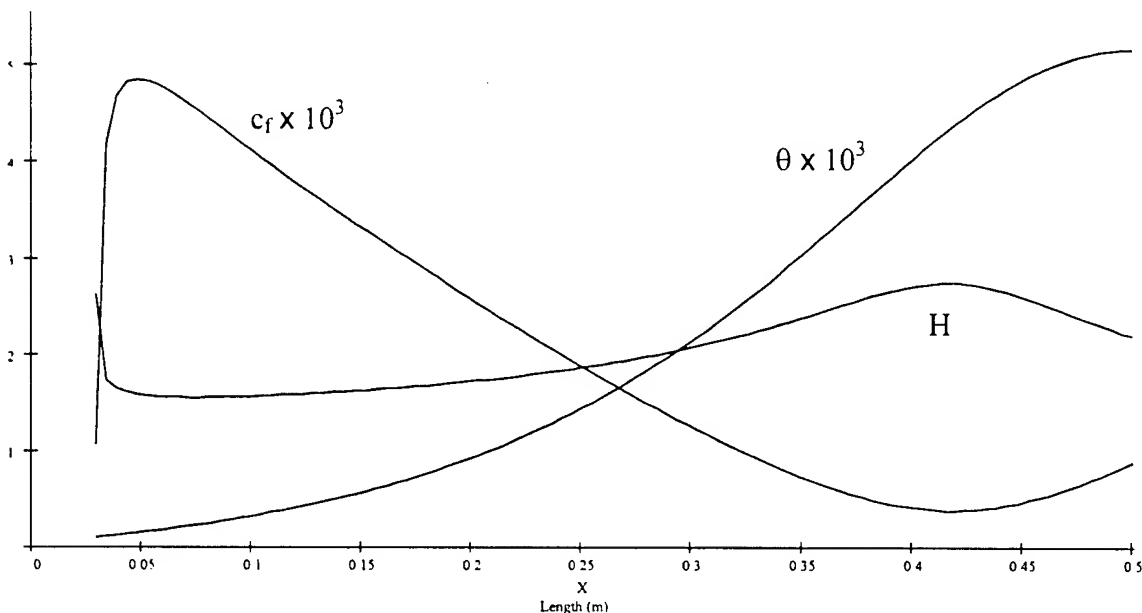


Figure 15 – Head Method Results for Decelerating Side of Laterally Offset Splitter Plate



Note the starting point of the curves is not at  $x=0$ , the beginning of the splitter plate, since these turbulent predictions begin at transition at about 6% of the splitter plate length (0.03m). Also note the immediate adjustment of shape factor and coefficient of friction from laminar values to turbulent values resulting from the solution to the differential equation. Recall that if  $c_f$  falls to zero, separation has occurred. These results show  $c_f$  reaching a minimum greater than zero at about 85% of the splitter plate length. Thus the length of the splitter plate, the velocity ratio and the lateral offset can be selected so that separation will not occur on the decelerating side of the splitter plate.

### Preliminary Measurements

The plane-mixing layer chosen to benchmark the Hartmann sensor will be achieved by inserting a splitter plate into the wind tunnel to divide the flow; one side will accelerate while the other side decelerates. The final design is shown in Figure 16. Among design considerations were material selection, support within wind tunnel without interfering with measurements, sufficient velocity ratio (high velocity over low velocity) without boundary layer separation, and sufficient thermal heating of air on one side of splitter plate so as to create thermal gradients in the mixing layer for imaging with the Hartmann sensor.

The splitter plate will be constructed of 18-gauge galvanized steel; this thickness is flexible but firm enough to hold its shape. The splitter plate will be supported with aluminum blocks sandwiching the corners of the sheet metal as seen in Figure 16. The primary purpose of the blocks are to hold the slope of

the plate as close to zero as possible along the edges, ensuring that the mixing layer will not be affected by unwanted flow structures. The hanging rods seen in Figure 16 are actually all-thread rods that have enabled us, by tapping the aluminum blocks, to vary the degree to which we can separate the flow. There are of course limitations; decelerating the flow too much on one side can cause a region of boundary layer separation, which would severely alter the mixing layer structures. A numerical model of the boundary layer growth on the decelerating flow side has been developed, and has estimated that a maximum offset of 2.5cm between front and back edges can be tolerated before separation will occur. Within our wind tunnel of 10cm width, this will generate a maximum velocity ratio of  $\sim 3.0$ , well within range of velocity ratios used by other experimentalists of which we will be comparing results for our benchmark.

Locating the aluminum holding blocks as far as possible from the vertical centerline and using minimal material will minimize flow interference of wakes behind the blocks and rods. Larger blocks and all-thread rods for the downstream locations are acceptable because their respective wakes do not develop quickly enough to interfere with the optical measurements, but do help to maintain the zero-slope requirement which is even more important off of the trailing edge. Lastly, since the Hartmann sensor measures index of refraction gradients within the flow, it was important to sufficiently heat one side of the splitter plate above the ambient temperature. Locating the leading edge of the splitter plate approximately 2 feet downstream from the onset of the heated sidewall will hopefully be far enough to achieve this.

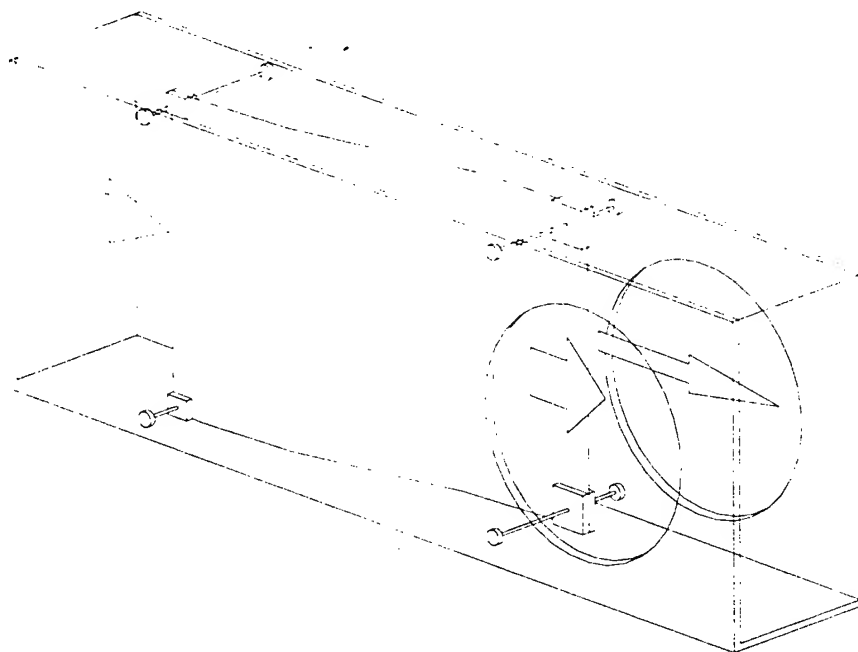


Figure 16 – Splitter plate in wind tunnel; arrows representing velocities in mixing layer at optical windows.

Hot-wire and cold-wire measurements will be made across the wind tunnel at the trailing edge to obtain velocity and temperature profiles, respectively. Hot/cold wire(s) support *within* the wind tunnel must be designed to allow the collection of data along the optical path, which is fundamental to the understanding of the Hartmann measurements. Since the windows fix the optical path location in the test-section, the splitter plate may be positioned at different downstream locations. This would allow measurements in the shear layer at different stages of its development. Once this benchmarking procedure has been performed and a firm relationship between flow structure and phasefront signature has been established, flow control surfaces will be mounted along the wind tunnel sidewalls or along the splitter plate. This optical diagnostic will provide detailed flow information for flow control studies.

In addition to the splitter plate to produce the mixing layer, a near-wall flow was created to examine turbulent structures with the Hartmann sensor. A cylinder was inserted into the wind tunnel in a cross-stream orientation and placed directly upstream of the imaged area of the Hartmann sensor. Figure 17 depicts the configuration; note the only the innermost region of the expanded laser beam is used to reduce diffraction interference from the iris aperture.

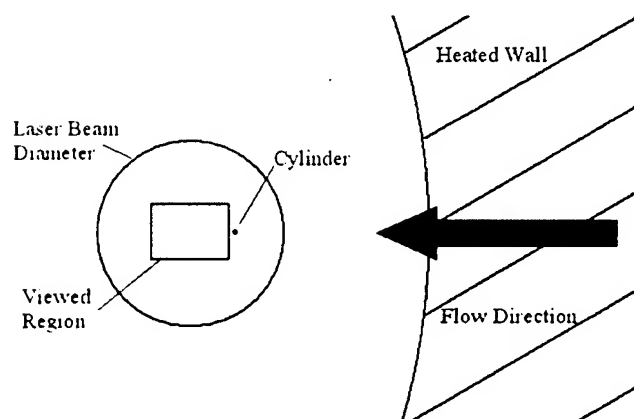


Figure 17 – Cylinder test case

Figure 18 shows an example of the focal spot displacements over the imaged area; the darker regions are areas of high phase shift and therefore are made up of high thermal gradients. As expected, vortex shedding was clearly visible downstream of the cylinder.

## Conclusion

A Hartmann wavefront sensor has been used to develop an optical diagnostic sensor for a custom wind tunnel with heated sidewalls. Relay – imaging optics have been incorporated into the optical train of the Hartmann sensor which optimize measurement sensitivity while allowing for variable spatial resolution of flow structures. A splitter plate has been modeled to design a shear layer flow to benchmark the optical diagnostic against a well-documented flow. Once complete, a system capable of measuring a turbulent mixing layer within a wind tunnel will be established and ready to undertake measurements of flow control flowfields.

## Acknowledgements

The assistance of Dr. Daniel R. Neal of Wavefront Sciences, Inc. is greatly appreciated.

Effort sponsored by the Air Force Office of Scientific Research, Air Force Material Command, USAF, under grant F49620-97-1-0417. The U.S. Government is authorized to reproduce and distribute reprints for Government purposes notwithstanding any copyright notation thereon.

The views and conclusions contained in this document are those of the author and should not be interpreted as necessarily representing the official policies or endorsements, either expressed or implied, of the Air Force Office of Scientific Research or the U.S. Government.

## References

- [1] Emrich, R.J., Editor, Methods of Experimental Physics, Vol. 18, Part A, New York, Academic Press, Inc., 1981, pp. 93-106
- [2] Neal, D. R., Hedlund, E., Lederer, M., Collier, A., Springs, C., Yanta, W., "Shack-Hartmann Wavefront Sensor Testing of Aero-Optic Phenomena", AIAA Paper 98-2701, June 1998
- [3] McMackin, L., Masson, B., Clark, K., Bishop, R., Chen, E., "Hartmann Wave Front Sensor Studies of Dynamic Organized Structure in Flowfields", AIAA Journal, Vol. 33, No. 11, Nov. 1995, pp. 2158-2164
- [4] Cebeci, T. & Bradshaw, P., Momentum Transfer in Boundary Layers, Washington, Hemisphere Publishing Corporation, 1977, pp. 192-194

- [5] White, F.M., Viscous Fluid Flow, 2<sup>nd</sup> edition, New York, McGraw-Hill, Inc., 1991, pp. 268-270, 358

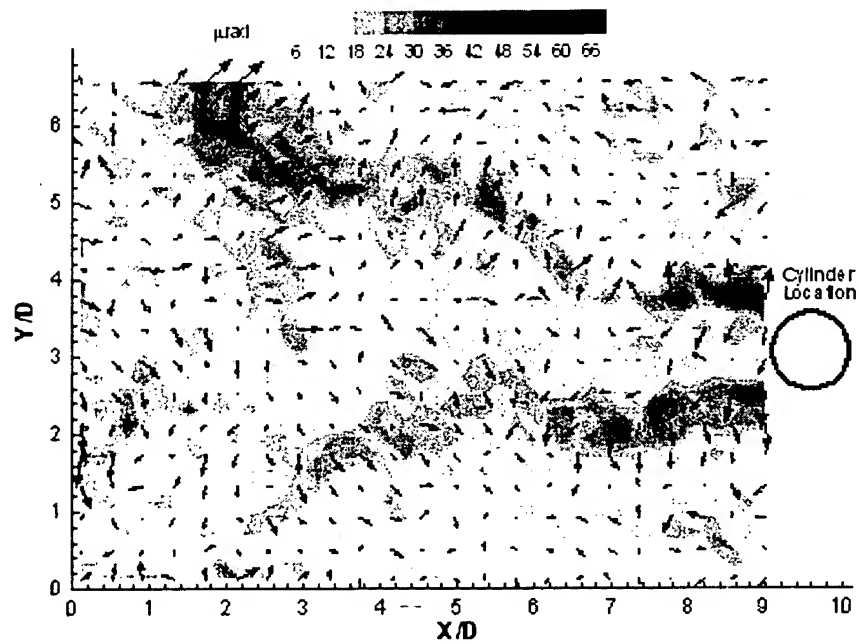


Figure 18 – Vortex shedding pattern behind cylinder